Current Topics in Electrochemistry
Vol. 22, 2020

Original Article

The multimodal dependence of anodic alumina film porous nanostructure on anodizing potential

G. Patermarakis*

Laboratory of Physical Chemistry, Department of Industrial Design and Production Engineering, School of Engineering, University of West Attica, P. Ralli & Thivon 250, Egaleo, Attiki, 11244, Greece.

ABSTRACT

The dependence of the nanostructure of porous anodic alumina films (PAAFs) on anodizing potential is useful in studies of PAAF growth kinetics and mechanism and for adjusting their structural properties for numerous applications often through linear dependencies that are not sufficiently justified. Suitable Al anodizing experiments were performed. Proper equations were formulated describing in steady state the dependence on the anodic potential P_{an} and the electrolysis voltage ΔV of PAAFs' main structural features, mean cell width D_c, pore base diameter D_p and barrier layer thickness *blt*. In the widest P_{an} and ΔV definition domains, retaining typical PAAF structure, these are implicit pseudo-linear equations, $D_c = f_c P_{an} = f_c \Delta V + g_c$, $D_p = f_p P_{an} = f_p \Delta V + g_p$ and $blt = f_b P_{an} = f_b \Delta V + g_b$, ($f_c$, f_p, $f_b > 0$), (g_c, g_p, $g_b < 0$), where f_c, f_p, f_b, g_c, g_p and g_b generally depend on many kinetic parameters, some of which depend in turn on P_{an}, ΔV or other additional parameters, some of which are interdependent etc. These equations describing the dependence of D_c, D_p and *blt* on P_{an} and ΔV become exact linear in anodizing regimes ensuring that all kinetic parameters defining f_c, f_p, f_b g_c, g_p and g_b are constant, which is rather impossible within such domains. If f_c, f_p, f_b, g_c, g_p and g_b change, the D_c, D_p and *blt* vs. P_{an} and ΔV plots deviate from linear by different modes, while each plot profile may differ from the rest. Experimental linear approximations refer to narrower domains, often for anodizing regimes giving the best hexagonal order of pores. The shift of domains produces changes in gradient and intercept. Moreover the intercept may become < 0 or ≥ 0. Linear or other monotonic D_c, D_p and *blt* vs. P_{an} or ΔV plots and exceptions are sufficiently explained for the first time. These results are important for Al anodizing electrochemistry and PAAF applications.

KEYWORDS: Al anodization, porous alumina films, nanostructure-potential dependence, equations.

1. INTRODUCTION

During Al anodization in pore-forming electrolytes, porous anodic alumina films (PAAFs) grow [1]. In such electrolytes, e.g. oxalic, sulphuric, phosphoric, tartaric, etc. acids, PAAFs grow in three sequential stages, the first and second transient stages and the steady state one. In steady state its structure is characterised as a close-packed array of about-hexagonal columnar cells [2-5]. Each cell contains an elongated roughly cylindrical pore vertical to the Al surface which extends from the metal|oxide interface to the top surface; among this interface and pore bottom the thin compact spherical sector shell-shaped barrier-type oxide layer with thickness about 1 nm per V of applied voltage is interposed [2-5].

Due to self-organized structure and specific electrochemical behaviour, Al anodizing has become an exciting model process in solid-state electrochemistry [3, 4, 6, 7]. Also PAAFs have become a fundamental tool to develop functional

*Email id: gpaterm@uniwa.gr

nanomaterials. PAAFs have specific structural, mechanical, physicochemical etc. properties, finding numerous applications in conventional engineering [7], modern science and nanoscience [6, 8-14] and currently developing technologies [15-21].

Linear (usually) or other monotonic dependencies of the main structural features of PAAFs on electrolysis (anodizing) voltage (ΔV) or on anodic potential (P_{an}) are reported in the literature for various electrolytes [5, 6, 22-27], which are not adequately explained yet. Linear dependency rules are generally used for tuning adjustable PAAF structural features. The main structural features are the mean cell width (D_c) correctly defined as the diameter of the circle with area identical to that of the mean cell, interpore distance (D_{int}, which is defined for hexagonally ordered porous structure as $D_{int} = D_c/1.05$), pore base diameter (D_p) and barrier layer thickness (*blt*). The pore surface density near Al (n) and D_c obey $n\pi(D_c^2/4) = 1$; thus they change oppositely. At given anodizing conditions, e.g. electrolyte type, concentration (c), temperature (T), etc., the structural features change when the current density in Al anode (j) or P_{an} or ΔV changes. The above dependencies refer generally to the steady state stage of film growth. Results are obtained for anodizing times (t), which can extend from the beginning of steady state up to much higher times. Noticeable results of linear or nonlinear dependencies are briefly presented below.

Al anodizing in H_3PO_4 electrolyte at c = 0.4 M, t = 60 min, T = 25 °C and constant ΔVs in the region 80–120 V, gave $D_c \approx 2.77\Delta V$, $blt \approx 1.04\Delta V$ and $D_p \approx 1.29\Delta V$ [22]. In H_2SO_4 at js in the region 0.5–50 mA cm^{-2}, t = 5–300 s corresponding to the initial range of steady state stage and ΔV varying from ≈ 2.5 V up to almost 20 V (that is a large enough range for this electrolyte), grouped results in each case ((c = 2M, T = 10, 20, 30 and 40 °C) and (T = 20 °C, c = 0.5, 1.0, 2.0 and 4.0 M)) were found to obey $D_c = 1.99\Delta V + 12.1$ nm [23]. In each case D_p is almost independent of ΔV in the region of lower ΔVs up to some higher ΔV value different in each case, after which it clearly increases, while *blt* increases monotonically with ΔV but the related plot bends to the right [23]. With H_2SO_4 20wt% electrolyte, ΔV = 15–25 V, T = 1 °C and ts ranged from 125 min at 25 V to 1,240 min at 15 V so that the obtained film thickness was 140 μm, reported data give $D_{int} \approx 3.2\Delta V$ - 12 nm and $D_p \approx 1.3\Delta V$ - 0.5 nm [24]. Also with H_2SO_4 20wt%, ΔV = 15–25 V and T = -8, 1 and 10 °C, D_{int} and D_p were found to obey relatively accurately D_{int} = (1.84, 2.10 and 1.87)ΔV + (12.23, 12.20 and 12.72) nm and D_p = (0.80, 0.53 and 0.72)ΔV + (1.06, 12.35 and 9.34) nm, respectively [25].

Collected data for several electrolytes and conditions showed usually linear dependencies of structural features on ΔV [6], but the gradients and intercepts seem to generally depend, more or less, on the electrolyte and specific anodizing regime. For H_2SO_4 electrolyte [5] at c = 1.53 M, j = 15 mA cm^{-2}, T = 20, 25 and 30 °C, various ts after the start of steady state at about 2 min and up to 30, 80 and 80 min, respectively, and P_{an}s in the range 10–20 V, the mean D_c at each T in steady state was found to obey $D_c \approx 2.1P_{an} + 12.6$ nm. At each T, P_{an} increased with t and approximate linear dependencies at these Ts gave $D_c \approx$ (4.6, 7.3 and 10.0)P_{an} - (27.7, 60.6 and 79.6) nm, respectively, thus with much different gradients and intercepts.

In $H_2C_2O_4$ electrolyte at j = 10 mA cm^{-2}, c = 0.60 M, T = 20 °C and t < 60 min in quasi-steady state ΔV gave a plateau ≈ 46 V. Then ΔV increased significantly to 54 V at 180 min and D_{int} changed as $D_{int} = 2.81\Delta V$ - 1.7 nm [26], which agrees with results in [19]. In $H_2C_2O_4$ a linear sweep voltammetry method was applied at c = 0.075–0.300 M (+ ethanol 5-10 vol. %), T = -1 to 0 °C prior to the start of anodization and up to a value below 3 °C during anodization and t = 90 min corresponding to the initial region of steady state [27]. Up to this t, ΔV increased to 120–225 V, then remained constant. Relatively accurate linear dependences $D_{int} = 2.4\Delta V$ - 44 nm, $blt = 1.1\Delta V$ - 12 nm were obtained, but D_p was kept almost constant around 50–60 nm.

In H_2SO_4 electrolyte at constant cs in the range 0.25–1.53 M, Ts in the range 0–35 °C, ΔV = 25 V (best ordering voltage regime for H_2SO_4 PAAFs [19, 28]) and t up to 90 min, the j vs. t plot had a highly variable profile in steady state [29]. At low cs and Ts, j was almost constant. But on increasing c and/or T the j vs. t plots gradually shifted upwards and left and concurrently presented high maxima due to significant change with t of *blt* and other related structural features, despite constant ΔV. Also, in this electrolyte at constant c, T, P_{an} and varying t up to 180 min, the j, ΔV, n, D_c and D_{int} changed

significant in steady state [30, 31]. These results along with the relative stability of some structural features while ΔV varies and deviation of the structural features vs. ΔV plots from linear ones in various ways in certain cases [23, 27], question the general reliability of linear or other monotonic dependence rules for quantitatively tuning the structural features.

Most often the linear or other monotonic plots refer to ΔV change. But $\Delta V = P_{an} + \Delta V_{bs} - P_{cath}$, where ΔV_{bs} is potential drop in bath solution and P_{cath} is cathodic potential (ΔV, P_{an} and $\Delta V_{bs} > 0$ and $P_{cath} < 0$). Each P_{an}, ΔV_{bs} and P_{cath} depends on current (I). When ΔV varies, P_{an}, ΔV_{bs} and P_{cath} are readjusted to satisfy this equation with common I. Thus I, j and mean current density in cathode (j_c) change. There is no reason for D_c, D_{int}, D_p and *blt* to depend on $\Delta V_{bs} - P_{cath}$. These must depend only on the potential drop in the barrier layer, which is not determinable and is inevitably approached by P_{an} (vs. SHE).

For each electrolyte many different Al anodizing regimes are possible. The simplest are shown in Table 1. The actual ones are many more, as more variable anodizing parameters and various experimental methods may be applied etc. Reasonably, the dependence of PAAF structure on anodizing potential must be somehow affected by anodizing regime.

The above point out the following still-open research subjects: (i_1) Explanation of the fact that gradients and intercepts of linear plots vary widely even for given electrolyte and identical or adjacent conditions. (ii_1) Explanation of the fact that at given c and T and various constant js or ΔVs or P_{an}s, the gradients and intercepts may differ strongly in plots of structural features vs. ΔV or P_{an} in the initial or later range of steady state and in plots for given j and various ts [5, 26, 27]. (iii_1) Rules to obtain representative results, helping to distinguish the real dependencies. (iv_1) Detection of any effect of $\Delta V_{bs} - P_{cath}$ in reported dependencies, unidentified heretofore. (v_1) Explanation of exceptions from linear or other monotonic increasing change of structural features with P_{an} or ΔV in certain anodizing regimes [29-31]. (vi_1) General explanation of results in each anodizing regime.

In this work, experimental results are obtained at suitable Al anodizing conditions which clearly dispute the general validity of the linear or other monotonic increase of the structural features with P_{an} and ΔV. Additional results for ΔV_{bs} and P_{cath} were also obtained within large ranges of anodizing parameters I and T, to determine the dependence of ΔV_{bs} and P_{cath} on I. Equations are formulated describing the actual dependence of PAAF structural features on P_{an} and ΔV and requirements are derived for linear dependencies. Predictions of equations are verified with present and previous literature results. Replies are given to open research subject queries. Lastly, an effective theory applicable to the study of PAAF growth kinetics and mechanism is developed.

2. MATERIALS AND METHODS

For thorough studies of the kinetics and mechanism of PAAF growth, thermostatically controlled three-electrode cell setup is necessary [29, 30, 32]. The setup used here is similar to that in [30, 31], consisting of upright Al working electrode and counter cathodic electrode (two Pb sheets symmetrically placed on either side of Al at distance 5 cm) and Hg/Hg_2SO_4 reference electrode. Al specimens with thickness 0.5 mm, purity $\geq$ 99.95% (Merck pro-analysis), dimensions of anodised surface 3×3 cm^2 and entire anodized surface area (S_g) 18.55 cm^2 [30] were used. The Pb cathodes (purity $\geq$ 99.968%, Merck pro-analysis) had thickness 0.5 mm, dimensions of conductive surface 5.5×5.5 cm^2 and total conductive surface (S_c) 122.05 cm^2. Al anodizing was performed in rigorously stirred H_2SO_4 electrolyte which is the most commonly used one.

A homemade power supply (Potentiostat – Automatic Reference Control – Model: PA–495) was used with upper limits of power output ≈ 50 W, current 2 A and voltage 32.5 V. Al was anodized at conditions c = 5% w/v (0.51 M), T = 25 (±0.1–0.2) °C, P_{an} = 23.615 V and ts $\leq$ 120 min with ΔV variable around 25 V, which defines the voltage regime that gives the best order of pores [19, 28], (case (v) in Table 1). Structural features of PAAFs were determined by field emission scanning electron microscopy (FESEM) (JEOL JSM -7401f). After selective removal of the oxide by chromo-phosphoric acid solution [3], the ns were found by counting the imprints of the cell/pore units in precisely determined Al surface areas. From ns, the

Table 1. Experimental conditions in the simplest applicable Al anodizing regimes for a given electrolyte. The anodizing parameters written in upright letters are the imposed ones and the parameters written in light italic letters are the ones produced during the experiments. The abbreviations p.s.s. and i.s.s.r. mean prolonged steady state and initial steady state range, respectively.

Aluminium anodizing regime	**Electrolyte concentration *c***	**Temperature *T***	**Current density *j***	**Time *t***	**Anodic potential P_{an}**	**Anodizing voltage ΔV**
(i)	constant	constant	constant	variable (p.s.s.)	*variable*	*variable*
(ii)	constant	variable	constant	*variable (i.s.s.r.)*	*variable*	*variable*
(iii)	variable	constant	constant	*variable (i.s.s.r.)*	*variable*	*variable*
(iv)	constant	constant	variable	*variable (i.s.s.r.)*	*variable*	*variable*
(v)	constant	constant	*variable*	variable (p.s.s.)	constant	*variable*
(vi)	constant	variable	*variable*	*variable (i.s.s.r.)*	constant	*variable*
(vii)	variable	constant	*variable*	*variable (i.s.s.r.)*	constant	*variable*
(viii)	constant	constant	*variable*	*variable (i.s.s.r.)*	variable	*variable*
(ix)	constant	constant	*variable*	variable (p.s.s.)	*variable*	constant
(x)	constant	variable	*variable*	*variable (i.s.s.r.)*	*variable*	constant
(xi)	variable	constant	*variable*	*variable (i.s.s.r.)*	*variable*	constant
(xii)	constant	constant	*variable*	*variable (i.s.s.r.)*	*variable*	variable

D_cs were then found. Other structure details were determined in films' fracture surfaces formed by bending Al specimens carrying the films.

Independent Al anodizing experiments were also conducted to study the cathodic potential and potential drop in bath bulk solution in wide ranges of *I*s and *T*s, irrespective of the detailed phenomena taking place in Al anode. The release of H_2 in cathode should also be examined, for which galvanostatic experiments serve better. Constant *I*s varying from 10 mA up to 2 A were applied. At each *T* the final maximum *I* was that at which one of the above limits of voltage or power output was reached first. The j, j_c, I, S_g and S_c are related by $j_c = I/S_c = jS_g/S_c = 0.152j$. At I = 10 mA, j = 0.55 mA cm^{-2} and j_c = 0.082 mA cm^{-2} and at I = 2 A, j = 107.82 mA cm^{-2} and j_c = 16.39 mA cm^{-2}. *I*s < 10 mA were not employed as the corresponding *j*s are very low, unsuitable for Al anodizing science and technology and PAAF applications.

The cathodic potential in Pb was measured with the pin mouth hole of reference electrode close to the Pb cathode, P_{cath} - P_{ref} (reference electrode close to cathode) = P_{cath} - P_{ref}(c). By definition $P_{cath} < 0$ and because $P_{ref} > 0$ (see below) P_{cath} - P_{ref}(c) < 0 always and at given conditions P_{cath} - P_{ref}(c) + P_{ref} = P_{cath}(vs. SHE(c)) = P_{cath} which is the real cathodic potential. P_{cath} - P_{ref} was also measured with the pin mouth hole of reference electrode close to the anode, P_{cath} - P_{ref} (reference electrode close to the anode) = P_{cath} - P_{ref}(a). It was < 0 but > P_{cath} - P_{ref}(c). The potential drop in solution from the anode to the cathodes (ΔV_{bs}) is thus ΔV_{bs} = [P_{cath} - P_{ref}(c)] - [P_{cath} - P_{ref}(a)] > 0. Then ΔV = [P_{an} - P_{ref}(a)] + ΔV_{bs} + [P_{ref}(c) - P_{cath}] = P_{an} + ΔV_{bs} - P_{cath} > 0, where P_{an} - P_{ref}(a) is the anodic potential vs. reference electrode attached close to Al anode.

Possible changes of P_{cath} - P_{ref}(c) and P_{cath} - P_{ref}(a) along the conductive Pb and anodized Al surfaces were studied. In each horizontal level crossing Pb, -P_{cath} + P_{ref}(c) > 0 was independent of reference electrode attachment position around Pb. The -P_{cath} + P_{ref}(c) value decreased slightly along the vertical surface of Pb cathode and upwards by e.g. ≈ 10 mV at I = 900 mA and T = 25 °C. Thus, -P_{cath} + P_{ref}(c) remains practically constant along the Pb surface. In each horizontal level crossing the anodised Al surface, the -P_{cath} + P_{ref}(a) > 0 value was also independent of reference electrode attachment position around the Al surface. But -P_{cath} + P_{ref}(a) increased perceptibly and almost linearly upwards by several tens of mV at this I and T. Then, measurements at

the middle of the narrow vertical side surface of Pb cathodes and Al anode were taken as tolerably representative. P_{cath}s and ΔV_{bs}s, determined at various *I*s (or j_cs) and T = 5, 15, 25 and 35 °C, and P_{ref} (vs. SHE) values at these *T*s 0.631, 0.623, 0.615 and 0.607 V [33] are used in the following analysis.

3. RESULTS AND DISCUSSION

3.1. Al anodizing at constant *c*, *T* and P_{an} and variable *t*. Results disputing the monotonic increase of structural features with P_{an} and ΔV. Important details of PAAF structure

In Fig. 1a-d the change of j, ΔV, n and D_c with t is shown at c = 0.51 M, T = 25 °C, P_{an} = 23.615 V and *t*s ≤ 120 min. The inset is a magnification of j vs. t plot at the very early stages of anodizing. The j abruptly rises, AB, then drops fast in the first transient stage BC. In BC a microscopically flat barrier type layer of oxide is formed; around point C, pores are nucleated on the oxide surface and the PAAF structure is generated [34-38]. In the second transient stage CD j rises, pores are developed and organized producing the PAAF structure [15-20, 36-41], completed around D [6, 22]. DE is the steady state that extends to higher *t*s DEFGHIJ where PAAF structure near the Al surface is reproduced and may remain (almost) stable or change.

In Fig. 1c FESEM micrographs of structural details at corresponding or indicated *t*s appear: imprints of cell/pore units on the Al surface (metal|oxide interface) at points D, G, H, I and J revealing their order; spherical sector-shaped ends to the Al side of columnar cells at H; section of cell/pore units around pore bases disclosing spherical sector shell-shaped barrier layer at G; section of pores and pore walls at distance from Al ≈ 23 μm (middle of film thickness) at H; section of pore walls and pores at distance from Al ≈ 92 μm (middle of thickness) showing termination and generation of pores.

The j rises in stage CD, then in stage DEFGHIJ a plateau DEFG with an imperceptible shallow minimum around F appears, followed by high peak around H. ΔV always lies around 25 V and generally follows j. In CD stage, D_c and ΔV rise and n drops while j rises. In DEFGHIJ stage, n and ΔV vary similarly and D_c inversely to j. Shallow j minimum at F implies that imperceptible n and ΔV minima and D_c maximum are expected, but practically, these remain constant in the plateau. The order of pores strongly improves in CD stage [31]. In DEFGHIJ stage, it is almost constant in DEFG region, worsens in the GH and improves from H to the end but remains inferior to DEFG. Changes in both structural features and pore ordering are related to continuous pore termination/generation processes at both stages [31] and additional inherent thinning of the mean barrier layer occurring exclusively at the second transient stage [22]. The much thinner pore walls at about the middle of the cross section of film at J than at H are mainly due to the much longer duration of chemical pore wall attack by the electrolyte.

Despite constant P_{an}, D_c and n vary in steady state. If linear or other monotonic increase of D_c and D_{int} with P_{an} or ΔV were valid, these should remain constant considering P_{an} or change similarly to ΔV, which is not the case.

Cross sections of barrier layer units formed by bending are rare in H_2SO_4 films [31]. Films crack through intercellular boundaries. Micrograph e.g. at j peak apex shows that cells are detached rather than fractured through planes containing pore axes. The spherical sector-shell barrier layer at G is compatible with the downer ends of detached cells shown at H.

Fig. 2 shows a schematic of the cell/pore unit around pore base. The D_c, D_p, blt and angle (φ) between pore axis and pore wall/barrier layer boundary are shown. Theoretically φ can change from 90° up to values well exceeding 90°. If φ = 90°, $blt = 2^{-1}(D_c - D_p)$, and the barrier layer is hemispherical. In general $blt = 2^{-1}(D_c - D_p)/\sin\varphi$ ($\varphi \geq 90°$), increasing with φ. In certain electrolyte(s) and anodizing conditions the actual shape of spherical sector shell-shaped barrier layer may be imperceptibly elliptic. For e.g. H_3PO_4 films, in the steady state growth of PAAF the thickness of barrier layer may be up to 5% higher in barrier layer/pore wall boundary than along pore axis as inferred from micrographs [22, 42], or ≈ 2.3% as predicted by steady state PAAF growth modelling [43, 44]. But its effect on PAAF growth modelling is truly negligible [45]. $\varphi \approx 136°$ [22, 43] and ≈ 127° [44, 45] were adopted with mean φ = 131.5°. Micrograph at G, Fig. 1c, predicts φ comparable to those values despite different electrolyte and conditions. Thus, change of φ with them, if any, is rather slight. For

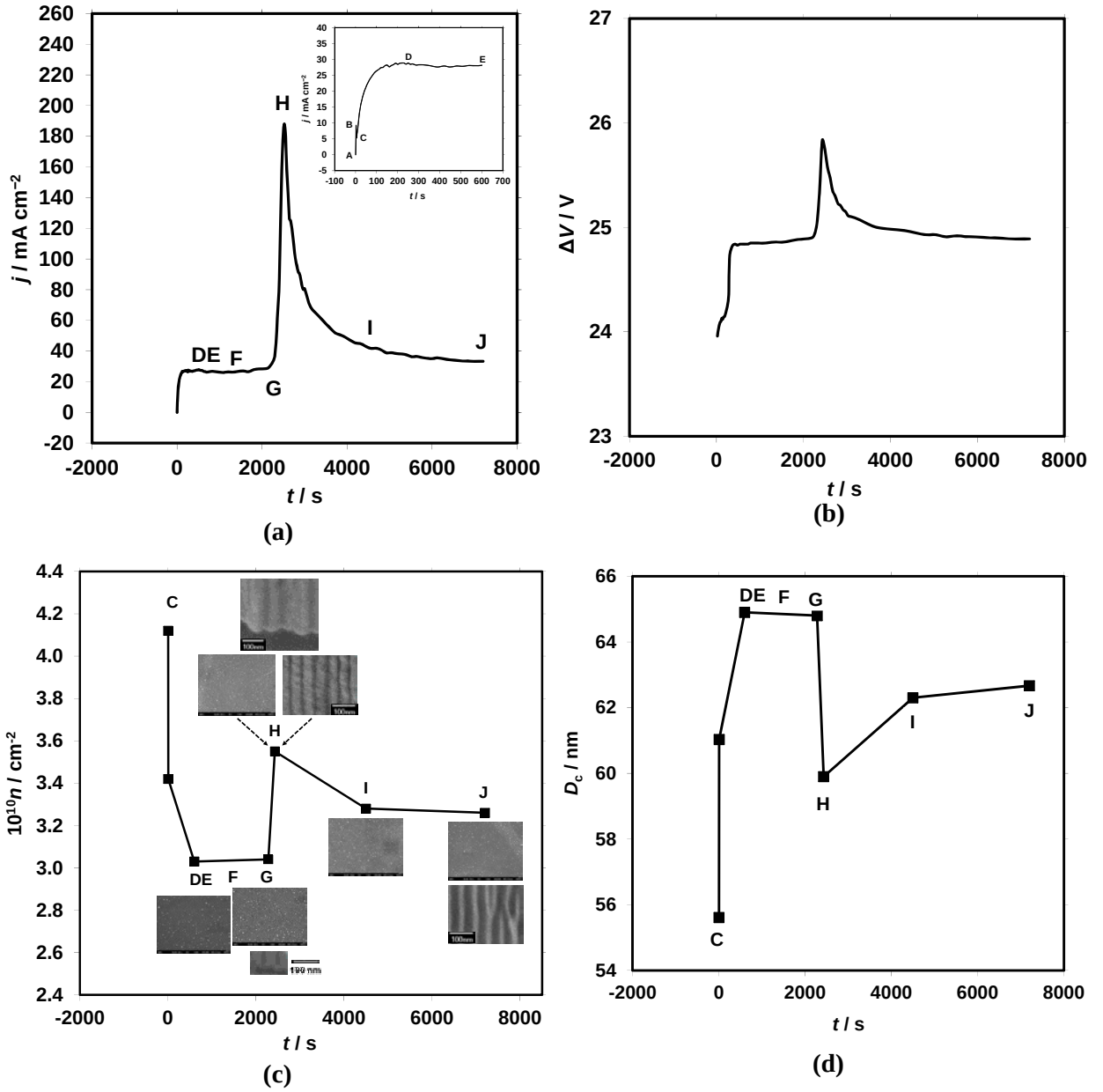

Fig. 1. Plots of (**a**) current density, j, (**b**) corresponding anodizing voltage, ΔV, (**c**) pore surface density near Al surface, n, and (**d**) mean cell width, D_c, vs. time, t, for Al anodizing at P_{an} (vs. SHE) = 23.615 V, $c(H_2SO_4)$ = 0.51 M and T = 25 °C. The inset in (a) is a magnification of j vs. t plot at the very early stages of anodizing. In (c) the inset FESEM micrographs at corresponding (or indicated) t's show PAAF structure details that are imprints of cell/pore units on the Al surface after the selective removal of oxide and fracture surfaces.

each anodizing electrolyte it can be considered to be about constant.

From the above and earlier results [5, 29-32] it seems that at constant e.g. j or ΔV or P_{an}, the ΔV and P_{an} or j and P_{an} or j and ΔV and other kinetic parameters and structural features of PAAF generally change slightly or significantly in steady state. Thus, it is actually a quasi-steady state. In the following, when referring to steady state, it is understood that the state is quasi-steady.

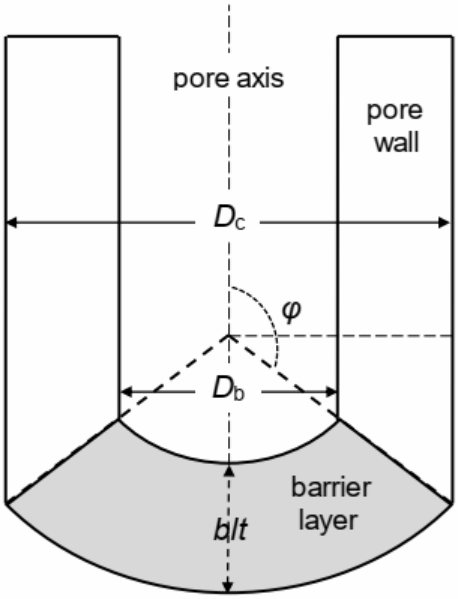

Fig. 2. Schematic cross section of a cell/pore unit of PAAFs around the pore base region. The pore, pore wall, barrier layer and its thickness, *blt*, angle of pore axis with the boundary of pore wall/barrier layer, φ, the cell width, D_c, and pore base diameter, D_p, are shown.

3.2. Dependencies of P_{cath} on j_c and T and of ΔV_{bs} on I and T

$-P_{cath}$ vs. j_c plots at various Ts appear in Fig. 3a which are sigmoid. P_{cath}s at given j_cs are generally comparable to those in the literature [46-48]. $-P_{cath}$ vs. $\ln j_c$ plots, Fig. 3b, are also sigmoid curves, typical for H_2 overpotential in Pb, Pt and other metals [46] which show two Tafel regions. Insets in Figs. 3a and b are magnifications of $-P_{cath}$ vs. j_c and $-P_{cath}$ vs. $\ln j_c$ plots in the range of lower employed j_cs which are curved. The successive regions of about-linear plots $-P_{cath}$ vs. j_c and $-P_{cath}$ vs. $\ln j_c$ (Tafel region) at low enough j_cs [46] must appear in this case at j_cs < 0.082 mA cm^{-2}. In the region of higher employed j_cs the Tafel equation $-P_{cath} = a + b\ln j$ satisfactorily applies, Fig. 3b. The values of a and b at different Ts are given in Table 2. The a shows a trend to drop and b shows a trend to rise on average with T, which agree with those for various other metals such as Hg, W etc. [46]. For j_cs including the values employed here, the overpotential of H_2 on Pb (and other metals such as Pt) and thus both a and b are almost independent of pH, thus also almost independent of c [46]. The rate determining step of H_2 release on Pb is thus electrochemical (not diffusion-limited) and the examination here of the overpotential dependence on c is unnecessary.

ΔV_{bs} vs. I plots at various Ts appear in Fig. 3c. At each T, $\Delta V_{bs} = IR_{bs}$ satisfactorily applies where R_{bs} (almost independent of I) is the total Ohmic resistance of the bath bulk solution during anodizing. This expected linear dependence in turn validates the method applied to find ΔV_{bs}s. R_{bs} thus found on average decreases slightly with T. This agrees with the relatively slight increase in conductivity of H_2SO_4 at the employed c and Ts in the range 5–35 °C [33]. The not-strictly linear ΔV_{bs} vs. I plots and non-strict monotonic variation of R_{bs} with T are due to coexistence of two phases in bath solution during anodizing, the conductive liquid H_2SO_4 solution and the non-conductive gaseous H_2 dispersed as gas bubbles in it. The amount of dispersed H_2 depends on I and T affecting R_{bs}. H_2 is accumulated more upwards due to buoyancy. Thus the conductivity of bath solution decreases (or the resistivity increases) along the vertical direction and upwards. It explains the perceptible rise of $[-P_{cath} + P_{ref}(a)] = \Delta V_{bs} + [-P_{cath} + P_{ref}(c)] > 0$ upwards along the Al surface and the slight fall of $-P_{cath} + P_{ref}(c) > 0$ upwards along the Pb surface. To a good approximation in Tafel region, $P_{an} = \Delta V - (\Delta V_{bs} - P_{cath}) = \Delta V - (IR_{bs} + a + b\ln j_c)$ or $\Delta V - P_{an} = \Delta V_{bs} - P_{cath} = IR_{bs} + a + b\ln j_c$.

Although $\Delta V_{bs} < -P_{cath}$, ΔV_{bs} is not negligible compared with $-P_{cath}$. $\Delta V_{bs} - P_{cath}$ = 0.37, 0.37, 0.38 and 0.38 V at the lowest and 1.42, 1.38, 1.62 and 1.58 V at the highest reached j_cs at T = 5, 15, 25 and 35 °C, respectively. ΔV values are 18.30, 9.00, 4.40 and 2.90 V at the lowest and 31.70, 32.30, 31.00 and 25.61 V at the highest j_cs at these Ts. Corresponding P_{an}s are 17.93, 8.63, 4.02 and 2.52 V at the lowest and 30.28, 30.92, 29.38 and 24.03 V at the highest j_cs, thus $\Delta V_{bs} - P_{cath}$ is 2.1, 4.3, 9.5 and 15.1% of P_{an} at the lowest and 4.5, 4.3, 5.2 and 6.5% of P_{an} at the highest j_cs. Though $P_{an} >> \Delta V_{bs} - P_{cath}$, $\Delta V_{bs} - P_{cath}$ is not negligible compared to P_{an}, mainly at high Ts and low j_cs, thus not ignorable.

The ionic conductor in bath solution has constant length, about double the distance of Al from each Pb electrode, through which $I/2$ current passes. For the given S_g and constant P_{an} or $I = jS_g = j_cS_c$, as S_c falls the mean section surface of conductor falls. Then j_c rises, ΔV_{bs} and $-P_{cath}$ also rise and $(\Delta V_{bs} - P_{cath})/P_{an}$ becomes significant. At a given ΔV, S_c

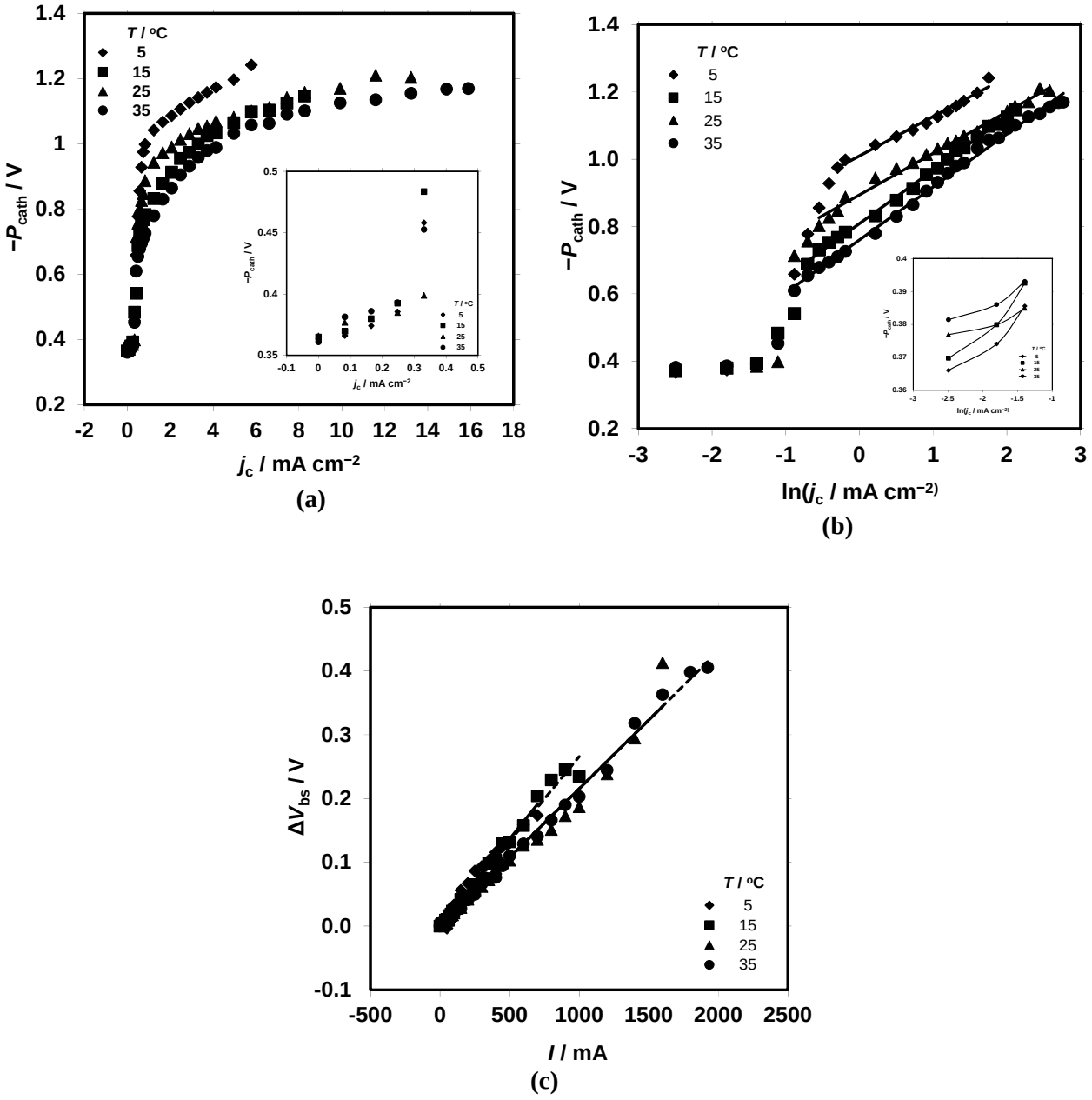

Fig. 3. Plots of the absolute cathodic potential, $-P_{cath}$, vs. current density in Pb cathodes, j_c, (**a**), of $-P_{cath}$ vs. ln (j_c/mA cm^{-2}) (**b**) and of the potential drop in bath bulk solution, ΔV_{bs}, vs. current, I, (**c**).

thus defines to a significant extent the real P_{an}. The relationship $-P_{cath} >> \Delta V_{bs}$, Fig. 3, may change in electrochemical cell setup with large distance between Al and cathode(s), low cs and/or Ts, less conductive electrolyte, etc. The fact that $\Delta V_{bs} - P_{cath}$ may be a significant portion of P_{an} is important when examining the dependence of PAAF structural features on ΔV.

3.3. Formulation of D_c, D_p and *blt* vs. P_{an} and ΔV equations

During the growth of PAAF at not excessively high js (thus release of O_2 gas in Al anode is avoided) the consumed Al closely obeys Faraday's law [29, 32]. Then the entire current through the barrier layer is almost totally ionic and the electronic current is negligible. It is accepted that only $O^{2-}$and Al^{3+} migrate

Table 2. Parameters a and b of Tafel equation ($-P_{cath} = a + b\ln j$) for hydrogen release in Pb cathodes, corresponding correlation coefficient, $CORR_1$, resistance of bath bulk solution, R_{bs}, found from ΔV_{bs} vs. I plots and corresponding correlation coefficient, $CORR_2$, during galvanostatic Al anodizing experiments.

T / °C	a / V	b / V	$CORR_1$	$10^{-1}R_{bs}$ / Ohm	$CORR_2$
5	1.010	0.117	0.991	2.73	0.987
15	0.809	0.158	0.999	2.66	0.994
25	0.894	0.123	0.995	2.15	0.987
35	0.760	0.157	0.998	2.16	0.998

in the barrier layer. Thus, the contribution to charge transport of the small amount of contaminant ionic species embodied in this layer is ignored, without injuring the ensuing analysis. For this analysis, the electrochemical kinetic equations describing the dependence of j and transport numbers of O^{2-} (tn_{an}) and Al^{3+} (tn_{ca}) ($tn_{ca} + tn_{an} = 1$) on the mean field strength across the barrier layer (E_{bl}) and the real anodizing temperature around the barrier layer (T_{an}) that exceeds T even slightly [29] are also necessary. In view of the above admissions these equations become

$$j = jtn_{an} + jtn_{ca} = A_2 \exp[(-W_2' + n_2 a_2 F E_{bl})/(RT_{an})] + A_3 \exp[(-W_3' + n_3 a_3 F E_{bl})/(RT_{an})]) \quad (1)$$

$$tn_{an} = jtn_{an}/(jtn_{an} + jtn_{ca}) = 1/\{1 + (A_3/A_2)\exp[(-W_3' + W_2' + (n_3 a_3 - n_2 a_2) F E_{bl})/(RT_{an})]\} \quad (2)$$

where A_2 and A_3 are pre-exponential factors of ionic O^{2-} and Al^{3+} currents defined by the product of physical constants and elementary parameters of statistical physical/thermodynamic and kinetic nature [29, 49], W_2' and W_3' are the apparent activation energies of O^{2-} and Al^{3+} migrations, n_2 and n_3 are the O^{2-} and Al^{3+} valences, a_2 and a_3 are the activation (half-jump) distances of O^{2-} and Al^{3+} transport, F is Faraday's constant and R is gas constant. For E_{bl} around 1 V nm^{-1}, $-W_2' + n_2 a_2 F E_{bl} > 0$ and $-W_3' + n_3 \alpha_3 F E_{bl} < 0$ [49]. Since $W_2' < W_3'$ [49], the rate controlling step is Al^{3+} transport. The a_2 and a_3 are comparable to O^{2-} and Al^{3+} radii 0.126 nm and 0.0535 nm [49], thus $n_3 a_3 - n_2 a_2 = 3a_3 - 2a_2 < 0$. Hence, $-W_3' + W_2' + (n_2 \alpha_2 F E_{bl} - n_3 \alpha_3) F E_{bl} < 0$. Considering constant A_2, A_3, W_2' and W_3', then tn_{an}, tn_{ca} and j are defined solely by E_{bl} and T_{an}.

Consistent with Eq. (1), j is very sensitive to E_{bl} changes. A small rise in E_{bl} produces large increase in j. The j is less sensitive to T_{an} changes and presents a shallow minimum at some T_{an} [32]. For example, at anodizing conditions in [32] change of E_{bl} by only ±0.733% around 1 V nm^{-1} affects j by ≈ ±6.6%. The required decrease in T_{an} in the left side and increase in T_{an} in the right side of this minimum for j increase ≈ 6.6% is ≈ 7.6%. Eq. (2) predicts that tn_{an} ($0 < tn_{an} < 1$) rises with E_{bl} but its rise is moderate, not as large as that of j. The tn_{an} also falls moderately with T_{an} e.g. for usual Ts in the range 0–40 °C. Predictions agree with results [49, 50].

There is not a simple equation describing $-P_{cath}$ in the whole range of j_cs employed. The js corresponding to the low j_cs up to near the start of Tafel region in Fig. 3b are generally low enough, not often used for Al anodizing and applications of PAAFs. Oppositely, the js corresponding to Tafel region of j_cs are those often used. To facilitate the ensuing analysis, the Tafel region of j_cs is considered. Thus at each T, $-P_{cath} = a + b\ln j_c$. From solution conductivity [33] and the expected PAAF thicknesses and mean porosities at various ts [30], the potential drop along the pores is found negligible compared with P_{an} [32]. There is no way to determine the exact potential drop across the barrier layer (ΔP), thus ΔP is inevitably approached by P_{an} ($\Delta P \approx P_{an}$).

For spherical sector shell-shaped barrier layer, ignoring other effects on E_{bl}, such as exact geometry details and dielectric behaviour of barrier layer, contaminant species embodied in this layer etc. [30],

$$E_{bl} = \Delta P / blt = \sin\varphi \Delta P / [2^{-1}(D_c - D_p)] \approx P_{an} / blt = \sin\varphi P_{an} / [2^{-1}(D_c - D_p)] \quad (3)$$

Since $P_{an} = \Delta V - (IR_{bs} + a + b\ln j_c)$

$$2^{-1}(D_c - D_p) = \sin\varphi E_{bl}^{-1} \Delta P \approx \sin\varphi E_{bl}^{-1} P_{an} = \sin\varphi E_{bl}^{-1} \Delta V - \sin\varphi E_{bl}^{-1}(IR_{bs} + a + b\ln j_c) \quad (4)$$

$$\text{or } 2^{-1}(D_c - D_p) = \alpha P_{an} = \alpha \Delta V - \beta \quad (5)$$

where $\alpha = \sin\varphi E_{bl}^{-1}$ and $\beta = \alpha(IR_{bs} + a + b\ln j_c) = \sin\varphi E_{bl}^{-1}(IR_{bs} + a + b\ln j_c)$, both > 0. Earlier [30, 31] it was also shown that

$$tn_{an} = 1 - (D_p / D_c)^2 \quad (6)$$

thus $tn_{ca} = (D_p/D_c)^2$, which coincides with film porosity around pore bases [51]. Eq. (6) is transformed to

$$2^{-1}(D_c - D_p) = 2^{-1}[1 - (1 - tn_{an})^{1/2}]D_c \quad (7)$$
$$\text{or } 1.05D_{int} = D_c = 2^{-1}(D_c - D_p)2[1 - (1 - tn_{an})^{1/2}]^{-1}$$

$$D_p = 2^{-1}(D_c - D_p)2[1 - (1 - tn_{an})^{1/2}]^{-1}(1 - tn_{an})^{1/2} = D_c(1 - tn_{an})^{1/2} \quad (8)$$

For usual values of tn_{an} = 0.5–0.95 [49, 50], the factors $(1 - tn_{an})^{1/2}$, $2^{-1}[1 - (1 - tn_{an})^{1/2}]$, $2[1 - (1 - tn_{an})^{1/2}]^{-1}$ and $2[1 - (1 - tn_{an})^{1/2}]^{-1}(1 - tn_{an})^{1/2}$ vary monotonically as 1.41–4.47, 0.71–2.24, 6.83–2.58 and 4.83–0.58, respectively. Eqs. (6)–(8) predict monotonic (may be linear) increase in always D_c and *blt* and usually D_p with P_{an} or ΔV. Considering e.g. constant *c* and *T*, as P_{an} or ΔV increases, in the first range of steady state *n* falls, D_c and *j* increase [24, 25, 27, 30] and tn_{an} does alike. $2^{-1}(D_c - D_p)$ increases, Eq. (7), and, considering almost constant φ, *blt* also increases. Though D_c increases, $(1 - tn_{an})^{1/2}$ decreases. Then, Eq. (8) shows that D_p can increase or remain almost constant (as often occurs [5, 6, 22-25, 27]), while a slight decrease cannot be excluded in some cases. Exceptions observed at constant *c*, *T* and P_{an}, Fig. 1, are also predicted by these equations. For almost constant T_{an}, when *j* and thus tn_{an} increases, E_{bl} increases, thus *blt* and $2^{-1}(D_c - D_p)$ decrease, Eqs. (1)–(3). Then both D_c and D_p decrease, Eqs. (7) and (8). Combination of Eqs. (3), (5), (7) and (8) gives

$$D_c = \alpha 2[1-(1-tn_{an})^{1/2}]^{-1}P_{an} = f_c P_{an} = \alpha 2[1-(1-tn_{an})^{1/2}]^{-1}\Delta V - \beta 2[1-(1-tn_{an})^{1/2}]^{-1} = f_c \Delta V + g_c \quad (9)$$

$$D_p = \alpha 2[1-(1-tn_{an})^{1/2}]^{-1}(1-tn_{an})^{1/2} P_{an} = f_p P_{an} = \alpha 2[1-(1-tn_{an})^{1/2}]^{-1}(1-tn_{an})^{1/2}\Delta V - \beta 2[1-(1-tn_{an})^{1/2}]^{-1}(1-tn_{an})^{1/2} = f_p \Delta V + g_p. \quad (10)$$

$$blt = (\sin\varphi)^{-1}2^{-1}(D_c - D_p) = (\sin\varphi)^{-1}\alpha P_{an} = f_b P_{an} = (\sin\varphi)^{-1}\alpha\Delta V - (\sin\varphi)^{-1}\beta = f_b \Delta V + g_b \quad (11)$$

The pre-potential factors f_c, f_p and f_b (> 0) are $f_c = \sin\varphi E_{bl}^{-1}2[1 - (1 - tn_{an})^{1/2}]^{-1}$, $f_p = \sin\varphi E_{bl}^{-1}2[1 - (1 - tn_{an})^{1/2}]^{-1}(1 - tn_{an})^{1/2}$ and $f_b = E_{bl}^{-1}$. The terms g_c, g_p and g_b (< 0) are $g_c = -\beta 2[1 - (1 - tn_{an})^{1/2}]^{-1}$, $g_p = -\beta 2[1 - (1 - tn_{an})^{1/2}]^{-1}(1 - tn_{an})^{1/2}$ and $g_b = -\beta(\sin\varphi)^{-1}$. Since $D_{int} = D_c/1.05$, D_{in} follows D_c. Because $n\pi(D_c^2/4) = 1$, by replacing D_c with $[4/(n\pi)]^{1/2}$ in Eq. (9), equations relating *n* with P_{an} and ΔV are also formulated. $\Delta V_{bs} - P_{cath} = IR_{bs} + a + b\ln j_c$ is embodied in g_c, g_p and g_b. Its role in related results is thus clarified. The f_c, f_p and f_b depend on the kinetic parameters E_{bl}, φ and T_{an} while g_c, g_p and g_b depend, besides E_{bl}, φ and T_{an}, also on *I*, R_{bs}, j_c, *a* and *b*. At least T_{an} depends on P_{an} and *j* as a result of heat production mainly around pore bases and its transfer to bath bulk solution *via* solid oxide and pore-filling solution [32], while *j* in turn depends on P_{an} *via* $E_{bl} \approx \sin\varphi P_{an}/[2^{-1}(D_c - D_p)]$ and Eq. (1). As ΔV changes the P_{an}, ΔV_{bs} and P_{cath} depending on the common *I* are readjusted to satisfy $\Delta V = P_{an} + \Delta V_{bs} - P_{cath}$, thus at least *I* and j_c depend on ΔV. Other kinetic parameters defining f_c, f_p, f_b, g_c, g_p and g_b can also interdepend.

Hence, as P_{an} and ΔV change, at least some of f_c, f_p, f_b, g_c, g_p and g_b depending indirectly on P_{an} and ΔV change too. Eqs. (9)–(11) are thus implicit and pseudo-linear. In the widest possible definition domains of P_{an} and ΔV, within which the characteristic cellular columnar porous structure is retained, strict linear dependencies of D_c, D_p and *blt* on P_{an} and ΔV may occur if all the above kinetic parameters remain constant. Such anodizing regime(s) seem impossible

or at most limited. These definition domains of P_{an} and ΔV are usually unknown or not examined. The equation $\Delta V_{bs} - P_{cath} = IR_{bs} + a + b\ln j_c$, embodied in Eqs. (9)–(11), is also a tolerable approximation and not a strict, as expected implicit, equation. Finally, experimental results of structural features vs. P_{an} and ΔV are usually obtained in anodizing regimes with narrower P_{an} and ΔV domains, mostly for the best hexagonal structure ordering, whereby satisfactory linear approximations may be possible.

The Eqs. (9)–(11) can be given in differential forms usable later

$$dD_c / dP_{an} = f_c + P_{an}(df_c / dP_{an}),\ dD_p / dP_{an} = f_p + P_{an}(df_p / dP_{an}),\ d(blt) / dP_{an} = f_b + P_{an}(df_b / dP_{an}) \quad (12)$$

$$dD_c / d(\Delta V) = f_c + \Delta V[df_c / d(\Delta V)] + dg_c / d(\Delta V),\ dD_p / d(\Delta V) = f_p + \Delta V[df_p / d(\Delta V)] + dg_p / d(\Delta V),$$
$$d(blt) / d(\Delta V) = f_b + \Delta V[df_b / d(\Delta V)] + dg_b / d(\Delta V) \quad (13)$$

In a relatively narrow range of P_{an} considering that f_c, f_p and f_b vary only slightly, $df_c/dP_{an} \approx 0$, $df_p/dP_{an} \approx 0$, $df_b/dP_{an} \approx 0$, and dD_c/dP_{an}, dD_p/dP_{an} and $d(blt)/dP_{an} \approx$ mean f_c, f_p and f_b or ≈ those at the middle of the range. Similarly, for slight changes in f_c, f_p, f_b, g_c, g_p and g_b within such narrow ΔV range, $df_c/d(\Delta V) \approx 0$, $df_p/d(\Delta V) \approx 0$, $df_b/d(\Delta V) \approx 0$, $dg_c/d(\Delta V) \approx 0$, $dg_p/d(\Delta V) \approx 0$, $dg_b/d(\Delta V) \approx 0$, and $dD_c/d(\Delta V)$, $dD_p/d(\Delta V)$ and $d(blt)/d(\Delta V) \approx$ mean f_c, f_p and f_b or ≈ those at the middle of ΔV range.

3.4. Required conditions for experimental linear dependencies of D_c, D_p and *blt* on P_{an} and ΔV

The complete requirements for accurate linear D_c, D_p and *blt* vs. P_{an} functions in an anodizing regime are: (a) as P_{an} rises, *n* falls; thus D_c rises; (b) the corresponding change of D_c, D_p and *blt* is much higher than experimental error of their determination; (c_1) constant f_c, f_p and f_b, which means constant α (or E_{bl} and φ) and tn_{an}; (d_1) intercepts of plots ≈ 0.

For simply satisfactory linear plots these become: (a); (b); (c_2) almost constant or slightly varying f_c, f_p and f_b; thus the same is valid for α (or E_{bl} and φ) and tn_{an}; (d_2) the intercepts of plots may deviate somewhat from 0 but not significantly.

Accurate linear D_c, D_p and *blt* vs. ΔV plots require: (a) where ΔV is considered instead of P_{an}; (b); (c_1); (d_3) constant g_c, g_p and g_b thus alike α (or E_{bl} and φ), tn_{an} and $\Delta V_{bs} - P_{cath} = IR_{bs} + a + b\ln j_c$, while $-g_c$, $-g_p$ and $-g_b$ << experimental D_c, D_p and *blt*, respectively.

For simply satisfactory linear plots vs. ΔV, requirements are: (a) as above; (b); (c_2); (d_4) almost constant or slightly varying g_c, g_p and g_b thus alike α (or E_{bl} and φ), tn_{an} and $\Delta V_{bs} - P_{cath}$, while $-g_c$, $-g_p$ and $-g_b$ << experimental D_c, D_p and *blt*.

Since strictly linear dependencies of structural features on P_{an} and ΔV in the widest definition domains of P_{an} and ΔV seem really impossible, the point is to evaluate the experimental dependencies in narrower ranges than these domains. If the requirements are satisfied, the linear functions are found from experimental results by regression analysis and their quality is estimated by common criteria. Some requirement(s) from (d_2)−(d_4) can be checked from the beginning, but (d_1) cannot. Finally, regression analysis can *ex post* affirm or deny (d_1)−(d_4). Requirements (a), (b), (c_1)−(c_4), (d_1), (d_2) and the first legs of (d_3) and (d_4) are clear, but the second legs of (d_3) and (d_4) need further assistive proof to become legible.

Always E_{bl} is about 1 V nm^{-1} [2–5]. Assuming mean $\varphi \approx 131.5°$, α is about 0.75 nm V^{-1}. In experiments at all *T*s and *j*s (section 3.2) $\Delta V_{bs} - P_{cath} \leq 1.62$ V, Fig. 3, then $\beta \leq 1.22$ nm. Also $\Delta V_{bs} - P_{cath}$ is a small portion of P_{an}, 2.1–15.1%. The $blt \approx$ (1 nm V^{-1}) ×(P_{an}), thus $\beta << blt$. For tn_{an} 0.5–0.95 [49, 50] $-g_c$ and $-g_p$ become at most ≈ 8.33–3.15 nm and ≈ 5.89–0.71 nm. Usually, $D_c \geq$ many tens up to hundreds of nm and $D_p \geq$ a few tens of nm up to many tens of nm [5, 6, 22-27], thus $-g_c << D_c$ and $-g_p << D_p$.

These are valid also for the electrolytes H_3PO_4, $H_2C_2O_4$ etc. that are less conductive than H_2SO_4. At identical *c*, *T* and *j*, $\Delta V_{bs} - P_{cath}$ is higher, but P_{an}, ΔV, *blt*, D_c and D_p are also higher [6, 22, 26, 27] and the second legs of (d_3) and (d_4) are satisfied too.

D_p generally varies slightly (as compared to D_c) with P_{an} and ΔV [5, 6, 22-25, 27], sometimes it is almost constant, while as previously noted a slight decrease cannot be excluded. These are due to the fact that $f_p < f_c$. For tn_{an} = 0.5–0.95 [49, 50] f_c and f_p are found to be $6.83\sin\varphi E_{bl}^{-1}$–$2.58\sin\varphi E_{bl}^{-1}$ and

$4.83\sin\varphi E_{bl}^{-1}$–$0.58\sin\varphi E_{bl}^{-1}$ while $f_b = E_{bl}^{-1}$. E_{bl} is always about 1 V nm^{-1} thus f_c and f_p depend mostly on tn_{an} and f_b depends solely on E_{bl}. Then, f_c and f_p decrease with tn_{an}. The ratio f_c/f_p is independent of E_{bl} and φ. It varies as (6.83/4.83)–(2.58/0.58) thus 1.41–4.47, justifying the larger variation of D_c than D_p. Especially at high tn_{an}s this ratio value becomes significant. The f_c/f_b varies as $6.83\sin\varphi$–$2.58\sin\varphi$ and f_p/f_b as $4.83\sin\varphi$–$0.58\sin\varphi$. The g_c and g_p vary as $[-6.83\sin\varphi E_{bl}^{-1}(\Delta V_{bs} - P_{cath})]$–$[-2.58\sin\varphi E_{bl}^{-1}(\Delta V_{bs} - P_{cath})]$ and $[-4.83\sin\varphi E_{bl}^{-1}(\Delta V_{bs} - P_{cath})]$–$[-0.58\sin\varphi E_{bl}^{-1}(\Delta V_{bs} - P_{cath})]$ while $g_b = -E_{bl}^{-1}(\Delta V_{bs} - P_{cath})$. The algebraic values of g_c and g_p increase with tn_{an}. The ratios of g_c, g_p and g_b vary as the corresponding ones of f_c, f_p and f_b.

3.5. Testing of the validity of formulated D_c, D_p and *blt* vs. P_{an} and ΔV equations. Explanation of experimental results

The validity of the formulated equations is first examined in terms of experimental literature D_c, D_p and *blt* vs. ΔV plots. Gradients are always > 0 for D_c and *blt*, as predicted. Gradient for D_p is usually ≥ 0; non-exclusion of gradient < 0 means that, while D_p obeys Eq. (10), f_p (> 0) concurrently depends on and falls significantly with ΔV. As shown earlier within relatively narrow P_{an} and ΔV ranges f_c, f_p, and f_b are almost constant, thus this is valid for f_c/f_p, f_c/f_b and f_p/f_b. If the accurate α (or E_{bl} and φ) values are unknown, then the f_c/f_p, f_c/f_b and f_p/f_b and therefore the ratios of plots' gradients can be used for comparisons. Even if α varies with ΔV, but not largely, its mean value can be considered in the employed ΔV range. Then these ratios serve for comparisons too. In [22], the ratio of gradients in D_c and D_p vs. ΔV plots is ≈ 2.77/1.29 ≈ 2.15. In [24] it is ≈3.2/1.3 ≈ 2.46. In [25] it is ≈1.05×1.84/0.8 ≈ 2.42, ≈1.05×2.1/0.53 ≈ 4.16 and ≈1.05×1.87/0.72 ≈ 2.73 at the employed *T*s. All ratios fall in the 1.41–4.47 range. For $\varphi \approx 131.5°$ and tn_{an} = 0.5–0.95, $f_c/f_b \approx$ 5.12–1.94, including the ratio of related plots' gradients in [27] that is 1.05×2.4/1.1 = 2.3.

In [5] the D_c and P_{an} that vary with *t* in steady state give D_c vs. P_{an} plots at different constant *T*s with (correctly) positive gradient. Gradient rises with *T*, mainly due to drop of tn_{an} with *T*, as Eq. (9) predicts.

The picture for intercepts differs very much. In [22] the intercepts are ≈ 0, in [23] reported values are > 0, in [24, 25] these are respectively < 0 and > 0 despite nearby anodizing conditions, in [26, 27] these are < 0 and in [5] these are > 0 for plots obtained at various *T*s and < 0 for plots obtained at various *t*s and for each employed *T*. But in Eqs. (9)–(11) g_c, g_p and g_b < 0. Results are also explainable. The f_c, f_p, f_b, g_c, g_p and g_b depend on a large number of kinetic parameters that may change in complex ways within an anodizing regime. Then, this is valid for f_c, f_p, f_b, g_c, g_p and g_b too. For ease, as examples, some cases from Table 1, with a limited number of variable kinetic parameters and with available experimental results, are discussed.

Experimental linear plots refer to P_{an} or ΔV ranges shorter than the widest definition domains. If in these domains results were available, e.g. for the cases (iv), (viii) and (xii) where P_{an}, ΔV and *j* together rise, real plots should bend to the right, Fig. 4 curve I. Along I the gradient of tangent falls with P_{an} or ΔV, while the intercept increases from < 0 to > 0 value. In a narrower P_{an} or ΔV range, the gradient and intercept of experimental linear plots of structural features vs. P_{an} or ΔV are approached by those of tangent at a point around the middle of this range and follow those of the tangent as the range shifts. Indeed, as shown earlier, in such a range of P_{an} dD_c/dP_{an} or dD_p/dP_{an} or $d(blt)/dP_{an} \approx$ f_c or f_p or f_b at the middle of P_{an} range. Similarly, $dD_c/d(\Delta V)$ or $dD_p/d(\Delta V)$ or $d(blt)/d(\Delta V) \approx f_c$ or f_p or f_b at the middle of ΔV range. Thus the tangent gradient ≈ this f_c or f_p or f_b. In both cases tangent intercept generally varies. For such ranges that shift to the right, it can be transformed from < 0 to > 0.

Such bending of large range plots, is mainly due to changes of *j* and tn_{an} with E_{bl} and T_{an}, Eqs. (1) and (2). As P_{an}, ΔV and *j* rise, E_{bl} and tn_{an} rise and f_c, f_p and f_b fall. T_{an} depends on the rates of heat production, mainly around the barrier layer, and its abduction to the solution. Thus it depends on *j*, P_{an} or ΔV and overall heat transport coefficient which in turn depends on film thickness, porosity, stirring rate etc. [32]. For high stirring rate and not very high *j*s, P_{an}s or ΔVs and thickness, T_{an} rises slightly with P_{an} or ΔV reducing tn_{an}. But the effect of E_{bl} dominates. In other cases the effect of T_{an} may dominate.

In [5] at constant *c*, *T* and *j* and various *t*s, case (i), P_{an}, ΔV and structural features change with *t*. The intercept of approximate linear D_c vs. P_{an} plot was < 0. In analogy to the above, at each *T* the D_c vs.

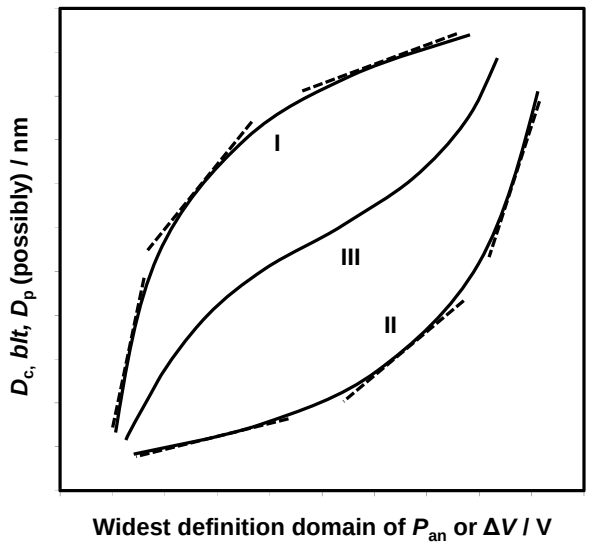

Fig. 4. Schematic curved dependencies of PAAF structural features on anodic potential, P_{an}, or anodizing voltage, ΔV, in their widest possible definition domain. The curves explain qualitatively the general multimodal dependence of structural features on the potential in three example cases. The broken lines represent the tangent line at various points. As the point of contact of the tangent to the curve shifts, both the gradient and intercept of the tangent change. The gradient and intercept of experimental linear plots, at a relatively narrow range around the point, change similarly. The multimodal dependence of the structural features on P_{an} and ΔV comes from concurrent change of the factors f_c, f_p and f_b and of the terms g_c, g_p and g_b in the implicit pseudo-linear Eqs. (9)–(11), with P_{an} and ΔV.

P_{an} plot in the widest definition domain must bend left, curve II, due mostly to T_{an} rise. As the thickness of film increases, the abduction of heat is hindered more, while the heat is released at a higher rate as P_{an} concurrently rises [32]. The gradient of tangent rises and intercept falls with P_{an} or ΔV, followed by those of experimental plots in a range shorter than the definition domain as the range shifts. In the employed P_{an} ranges, the intercept is < 0. Its fall with T is due to the simultaneous shift and turn to the left of curve II, so that generally the gradient increases and intercept decreases. This also holds for the employed P_{an} ranges [5].

Each of f_c, f_p and f_b is affected by kinetic parameters to different extents. Each of g_c, g_p and g_b alike is affected by more kinetic parameters. The profile of each structural feature vs. P_{an} or ΔV plot may thus differ from the other ones, mainly in large P_{an} or ΔV ranges. In [23] (case (iv) at various Ts and cs) the D_c vs. ΔV plot is approximately linear but the D_p and blt vs. ΔV plots bend left and right, respectively. For D_p, plot bending, occurring mainly in the region of high ΔVs and js, is due to significant rise of T_{an}, the effect of which on tn_{an} now dominates. For blt, plot bending is due to the increase of E_{bl} (or due to the decrease of $f_b = E_{bl}^{-1}$) with ΔV and j. In anodizing regimes with more variable anodizing parameters, the f_c, f_p, f_b, g_c, g_p and g_b must be affected by more variable kinetic parameters. In the widest definition domains, real plots may be more complex, such as curve III, etc. D_p may even fall monotonically or change in another way. In these cases the explanations become more complex.

As shown in section 3.3 the exception from monotonic or linear increase of D_c, D_p and blt with P_{an} or ΔV at constant P_{an}, c and T and variable t (case (v)), Fig. 1, is also compatible with Eqs. (9)–(11). In DG region the rates of incessant pore termination/generation processes are least and balanced, as shown by the micrograph at the middle of film cross section at H. It shows porous structure just above metal|oxide interface when the film had thickness $\approx$ 23 μm (half that at H). The 23 μm thickness is formed at t within DG. Termination or generation of pores is not detected. In DG region the structural features are expected to be embodied in linear or other monotonic plots of D_c and blt (and presumably of D_p) vs. P_{an} or ΔV for various P_{an}s, case (viii). But, from G to H pore generation dominates and after H termination does. At H, Fig. 1c–d, maxima of tn_{an} and n and minima of D_c, D_p and blt appear. While P_{an} is constant and ΔV rises, n increases. Thus, the requirement (a) is not satisfied, justifying the exception. This change of n at prolonged anodizing is explained as follows.

Beyond G the significant increase in film thickness favours appreciable T_{an} rise and accumulation of Al^{3+} and electrolyte anions around pore bases [52, 53], which must be among the main factors favouring pore branching inwards and n rise. Thickening beyond H causes further T_{an} rise and significant mass transfer retardation due to lengthy pores some of which become labyrinthine by termination/ generation processes. Excessive accumulation of such species produces colloidal nanoparticles [54]

(made of Al^{3+}, electrolyte anions, H_2O and OH^-) and complex cations $Al(OH)^{2+}$, $Al(OH)_2^+$, $Al_2(OH)_2^{4+}$, $Al_3(OH)_6^{3+}$, $Al[(OH)_5Al_2]_n^{(n+3)+}$, $Al_6(OH)_{15}^{3+}$ etc. [55, 56], that are less mobile than H^+ [33]. Their intense presence at pore bases seems to hinder generation of new pores and favor termination. Structure changes are expected until attainment of maximum limiting mean film thickness, pore length, porosity and species concentrations at pore bases, beyond J as plots in Fig. 1 predict. Solution composition at pore bases affects these processes, just as the electrolyte type defines the growth of porous or nonporous films or pitting [51].

Nucleation of pores [57] occurs around C, Fig. 1. Then termination of pores dominates over generation up to about D [31]. Constant D_c, D_p and *blt* at constant P_{an} or ΔV are possible when the rates of pore generation/termination are balanced or ≈ 0. This occurs in DG region, supporting the rule that structural features in the first range of steady state must be taken into consideration in order to reveal their real dependencies on P_{an} or ΔV. The *t* must lie in this range but it may not be constant as *t*(D) varies e.g. with *c*, *T*, *j*, P_{an} and ΔV. The results in all other cases of Table 1 or in other even more complex cases are explained by analyses similar to the above.

4. CONCLUSIONS

From this investigation the main concluding remarks are the following:

1. In steady state of PAAF growth, the structural features obey implicit pseudo-linear equations $D_c = f_c P_{an} = f_c \Delta V + g_c$, $D_p = f_p P_{an} = f_p \Delta V + g_p$ and $blt = f_b P_{an} = f_b \Delta V + g_b$. The f_b (> 0) depends on field strength and angle between pore axis and barrier layer/pore wall boundary, f_c and f_p (> 0) depend also on O^{2-} transport number in barrier layer and the g_c, g_p and g_b (< 0) moreover on current, solution resistance, current density in cathode and H_2 release Tafel parameters. Some parameters defining f_c, f_p, f_b, g_c, g_p and g_b depend in turn on P_{an} and ΔV and other interdepend. So, f_c, f_p, f_b, g_c, g_p and g_b change with P_{an} or ΔV by various modes. Linear or other one-type monotonic increase of D_c or D_{int}, *blt* and D_p with P_{an} or ΔV is not assured.
2. The monotonic or linear increase of D_c or D_{int}, D_p and *blt* with P_{an} or ΔV, when existing, cannot be artificially created by ΔV_{bs} - P_{cath} included in ΔV. ΔV_{bs} - P_{cath} is embodied in g_c, g_p and g_b.
3. Requirements for linear plots of structural features vs. P_{an} or ΔV, obeying the above equations, were formulated. In the widest P_{an} (or ΔV) definition domains, maintaining the characteristic PAAF structure, exact linear plots, thus constant f_c, f_p and f_b with g_c, g_p and $g_b \approx 0$ (or constant f_c, f_p, f_b, g_c, g_p and g_b), seem rather impossible. Almost constant or slightly changing kinetic parameters may yield tolerable linear plots in ranges of P_{an} or ΔV narrower than these domains.
4. For anodizing regimes which do not assure constant f_c, f_p, f_b, g_c, g_p and g_b in the widest P_{an} (or ΔV) domains, each D_c, D_p and *blt* vs. P_{an} or ΔV plot deviates from linear in various ways and the dependence of D_c, D_p and *blt* on P_{an} or ΔV is in fact multimodal.
5. Tolerable experimental linear structural features vs. P_{an} or ΔV plots, often associated with hexagonal maximum pore ordering, actually refer to ranges of P_{an} and ΔV narrower that definition domains. Even for the same electrolyte and neighboring anodizing conditions, gradients and intercepts of plots can thus vary and intercept can be either ≤ 0 or > 0.
6. Monotonic increase of D_c with P_{an} and ΔV means decrease of *n* with them. Exceptions are observed e.g. during prolonged Al anodizing at constant P_{an} where *n* varies similarly to *j* and ΔV while D_c, D_p and *blt* vary inversely. These are due to unstable *n*, coming from continuous pore termination/generation processes as a result of altered conditions at pore bases.
7. The experimental linear or other monotonic dependencies of D_c, D_p and *blt* vs. P_{an} or ΔV and exceptions were adequately explained for the first time. A novel theoretical tool was presented, revealing the real dependence of PAAF structure on anodizing potential, important for the Al anodizing electrochemistry and numerous PAAF applications.

CONFLICT OF INTEREST STATEMENT

The author declares no conflict of interest.

ABBREVIATIONS

a_2 and a_3	=	Activation (half jump) distances of O^{2-} and Al^{3+} transport inside the barrier layer (nm).

a and b	=	Tafel parameters for hydrogen evolution on cathodes.
α (Greek)	=	E_{bl}^{-1}.
β (Greek)	=	$(IR_{bs} + a + b\ln j_c)E_{bl}^{-1}$.
A_2 and A_3	=	Pre-exponential factors in Eqs. (1) and (2) (mA cm^{-2}).
blt	=	Barrier layer thickness (nm).
c	=	Concentration of H_2SO_4 or other anodizing electrolyte (M).
D_c, D_{int} and D_p	=	mean cell width, interpore distance and pore base diameter (nm).
ΔP	=	Potential drop across the barrier layer (V).
ΔV	=	anodizing voltage (V).
ΔV_{bs}	=	Potential drop in bath solution between Al anode and Pb cathodes (V).
E_{bl}	=	Mean high field strength across the barrier layer (V nm^{-1}).
f_c	=	$\sin\varphi E_{bl}^{-1}2[1 - (1 - tn_{an})^{1/2}]^{-1}$, (> 0), (nm V^{-1}).
f_p	=	$\sin\varphi E_{bl}^{-1}2[1 - (1 - tn_{an})^{1/2}]^{-1}(1 - tn_{an})^{1/2}$, (> 0), (nm V^{-1}).
f_b	=	E_{bl}^{-1}, (> 0), (nm V^{-1}).
φ	=	angle between pore axis and barrier layer/pore wall boundary.
F	=	Faraday's constant (96487 C mol^{-1}).
FESEM	=	Field Emission Scanning Electron Microscopy.
g_c	=	$-\beta 2[1 - (1 - tn_{an})^{1/2}]^{-1}$, (< 0), (nm).
g_p	=	$-\beta 2[1 - (1- tn_{an})^{1/2}]^{-1}$ $(1 - tn_{an})^{1/2}$, (< 0), (nm).
g_b	=	$-(\sin\varphi)^{-1}\beta$, (< 0), (nm).
I	=	$jS_g = j_cS_c$ = Current (A).
j	=	Current density in Al anode (mA cm^{-2}).
j_c	=	Current density in cathodes (mA cm^{-2}).
n	=	Surface density of oxide cell/pore units near the Al substrate surface (cm^{-2}).
n_2 and n_3	=	Valences of O^{2-} and Al^{3+} ions.
PAAF	=	Porous anodic alumina film.
P_{an}	=	Anodic potential vs. SHE (V).
P_{cath}	=	Cathodic potential vs. SHE (V).
$P_{an} - P_{ref}$(a)	=	Potential difference between Al anode and reference electrode close to anode (V).
$P_{cath} - P_{ref}$(a)	=	Potential difference between cathode and reference electrode close to anode (V).
$P_{cath} - P_{ref}$(c)	=	Potential difference between cathode and reference electrode close to cathode (V).
R	=	Universal gas constant (8.314 J K^{-1} mol^{-1}).
R_{bs}	=	Resistance of bath bulk solution during Al anodizing (Ohm).
S_c	=	Total conductive geometric surface area of two Pb cathodes where H_2 is released (cm^2).
S_g	=	Geometric surface area of Al specimens that is oxidized during anodizing (cm^2).
t	=	anodizing time (min or s).
tn_{an} and tn_{ca}	=	Transport numbers of O^{2-} and Al^{3+} across the barrier layer (dimensionless).
T	=	Temperature of bath bulk solution (°C or K).
T_{an}	=	Real anodizing temperature in the barrier layer region (°C or K).
W_2' and W_3'	=	Apparent activation energies of O^{2-} and Al^{3+} transport across the barrier layer (J mol^{-1}).

REFERENCES

1. Lee, W. and Park, S. J. 2014, Chem. Rev., 114(15), 7487.
2. Keller, F., Hunter, M. S. and Robinson, D. L. 1953, J. Electrochem. Soc., 100(9), 411.
3. Young, L. 1961, Anodic Oxide Films, Academic Press, London.
4. Diggle, J. W., Downie, T. C. and Goulding, C. W. 1969, Chem. Rev., 69(3), 365.
5. Patermarakis, G. and Moussoutzanis, K. 2011, J. Electroanal. Chem., 659(2), 176.
6. Sulka, G. D. 2008, Nanostructured Materials in Electrochemistry, A. Eftekhari, Ed., John Wiley and Sons, Wienheim, 1.
7. Sheasby, P. G. and Pinner, R. 2001, The Surface Treatment and Finishing of Aluminum and Its Alloys, ASM International & Finishing Publications Ltd., USA-UK.
8. Martin, C. R. 1996, Chem. Mater., 8(8), 1739.
9. Kovtyukhova, N. I. and Mallouk, T. E. 2005, Adv. Mater., 17(2), 187.
10. Ganley, J. C., Riechmann, K. L., Seebauer, E. G. and Masel, R. I. 2004, J. Catal., 227(1), 26.
11. Pellin, M. J., Stair, P. C., Xiong, G., Elam, J. W., Birrell, J., Curtiss, L., George, S. M., Han, C. Y., Iton, L., Kung, H., Kung, M. and Wang, H. H. 2005, Catal. Lett., 102(3-4), 127.
12. Burgos, N., Paulis, M. and Montes, M. 2003, J. Mater. Chem., 13(6), 1458.
13. Das, G., Patra, N., Gopalakrishnan, A., Zaccaria, R. P., Toma, A., Thorat, S., Di Fabrizio, E., Diaspro, A. and Salerno, M. 2012, Analyst, 137(8), 1785.
14. Toccafondi, C., La Rocca, R., Scarpellini, A., Salerno, M., Das, G. and Dante, S. 2015, Appl. Surf. Sci., 351, 738.
15. Jessensky, O., Muller, F. and Gösele, U. 1998, Appl. Phys. Lett., 72(10), 1173.
16. Zhang, L., Cho, H. S., Li, F., Metzger, R. M. and Doyle, W. D. 1998, J. Mater. Sci. Lett., 17(4), 291.
17. Jessensky, O., Muller, F. and Gösele, U. 1998, J. Electrochem. Soc., 145(11), 3735.
18. Nielsch, K., Choi, J., Schwirn, K., Wehrspohn, R. B., and Gösele, U. 2002, Nano Lett., 2(7), 677.
19. Li, A. P., Muller, F., Bimer, A., Nielsch, K. and Gösele, U. 1998, J. Appl. Phys., 84(11), 6023.
20. Li, A. P., Müller, F. and Gösele, U. 2000, Electrochem. Solid-State Lett., 3(3), 131.
21. Napolskii, K. S., Roslyakov, I. V., Eliseev, A. A., Petukhov, A. V., Byelov, D. V., Grigoryeva, N. A., Bouwman, W. G., Lukashin, A. V., Kvashnina, K. O., Chumakov, A. P., and Grigoriev, S. V. 2010, J. Appl. Crystallog., 43(3), 531.
22. O'Sullivan, J. P. and Wood, G. C. 1970, Proc. Roy. Soc. Ser. A Math. Phys. Sci., 317(1531), 511.
23. Ebihara, K., Takahashi, H., and Nagayama, M. 1982, J. Met. Finish. Soc. Jpn., 33(4), 156.
24. Sulka, G. D., Stroobants, S., Moshchalkov, V., Borghs, G., and Celis, J. P. 2002, J. Electrochem. Soc., 149(7), D97.
25. Sulka, G. D. and Parkoła, K. G. 2007, Electrochim. Acta, 52(5), 1880.
26. Montero-Moreno, J. M., Sarret, M. and Müller, C. 2010, Microporous Mesoporous Mater., 136(1-3), 68.
27. Vega, V., García, J., Montero-Moreno, J. M., Hernando, B., Bachmann, J., Prida, V. M. and Nielsch, K. 2015, ACS Appl. Mater. Interfaces, 7(51), 28682.
28. Masuda, H., Hasegwa, F. and Ono, S. 1997, J. Electrochem. Soc., 144(5), L127.
29. Patermarakis, G. and Kapiris, G. 2013, J. Solid State Electrochem., 17(4), 1133.
30. Patermarakis, G. and Plytas, J. 2016, J. Electroanal. Chem., 769, 97.
31. Patermarakis, G. and Triantis T. M. 2019, Curr. Top. Electrochem., 21, 21.
32. Patermarakis, G. 2014, J. Electroanal. Chem., 730, 69.
33. Dobos, D. 1975, Electrochemical Data: A Handbook for Electrochemists in Industry and Universities, Elsevier.
34. Surganov, V. F. and Gorokh, G. G. 1993, Mater. Lett., 17(3-4), 121.
35. Surganov, V., Jansson, C., Nielsen, J. G., Morgen, P., Gorokh, G. and Larsen, A. N. 1988, Electrochim. Acta, 33(4), 517.
36. Dell'Oca, C. J. and Fleming, P. J. 1976, J. Electrochem. Soc., 123(10), 1487.
37. Parkhutik, V. P. 1986, Corros. Sci., 26(4), 295.
38. Parkhutik, V. P. and Shershulsky, V. I. 1992, J. Phys. D, 25(8), 1258.

39. Patermarakis, G., Chandrinos, J. and Masavetas, K. 2007, J. Solid State Electrochem., 11(9), 1191.
40. Masuda, H., Yotsuya, M., Asano, M., Nishio, K., Nakao, M., Yokoo, A. and Tamamura, T. 2001, Appl. Phys. Lett., 78(6), 826.
41. Pan, H., Lin, J., Feng, Y. and Gao, H. 2004, IEEE Trans. Nanotechnol., 3(4), 462.
42. Thompson, G. E. and Wood, G. C. 1983, Treatise on Materials Science and Technology, Vol. 23, J. C. Scully (Ed.), Academic, New York, 205.
43. Houser, J. E. and Hebert, K. R. 2006, J. Electrochem. Soc., 153 (12), B566.
44. Houser, J. E. and Hebert, K. R. 2007, ECS Transactions, 3(31), 375.
45. Mirzoev R. A., Davydov, A. D., Zarubenko, E. S., Vystupov, S. I. and Panteleev, E. S. 2016, Electrochim. Acta, 218, 74.
46. Antropov, L. 1972, Theoretical Electrochemistry, Mir Publishers, Moscow.
47. Koryta, J., Dvorak, J. and Bohackova, V. 1970, Electrochemistry, Methuen, London.
48. Davies, C. W. 1967, Electrochemistry, Newnes, London.
49. Patermarakis, G. and Diakonikolaou, J. 2012, J. Solid State Electrochem., 16(9), 2921.
50. Patermarakis, G. and Moussoutzanis, K. 2009, Electrochim. Acta, 54(9), 2434.
51. Mirzoev, R. A., Davydov, A. D., Vystupov, S. I. and Kabanova, T. B. 2019, Electrochim. Acta, 294, 276.
52. Patermarakis, G. 1998, J. Electroanal. Chem., 447, 25.
53. Patermarakis, G. and Moussoutzanis, K. 2001, Corros. Sci., 43, 1433.
54. Patermarakis, G. and Moussoutzanis, K. 2002, J. Solid State Electrochem., 6(7), 475.
55. Vogel, A. I. 1976, Macro and Semimicro Quantitative Analysis, Longman, London.
56. Alexeyev, V. N. 1980, Qualitative Chemical Analysis, Mir Publishers, Moscow.
57. Patermarakis, G. 2009, J. Electroanal. Chem., 635(1), 39.